Steel and Composite Structures, *Vol. 18, No. 6 (2015) 1517-1539*
DOI: http://dx.doi.org/10.12989/scs.2015.18.6.1517

Seismic performance of eccentrically braced frames with high strength steel combination

Ming Lian *, Mingzhou Su and Yan Guo

College of Civil Engineering, Xi'an University of Architecture and Technology, Xi'an 710055, P.R. China

(*Received March 21, 2014, Revised September 03, 2014, Accepted December 09, 2014*)

Abstract. Eccentrically braced frames (EBFs) often use conventional steel with medium yield strength. This system requires structural members with large cross-sections for well seismic behavior, which leads to increased material costs. In eccentrically braced frames with high strength steel combination (HSS-EBFs), links use Q345 steel (specified nominal yield strength 345 MPa), braces use Q345 steel or high strength steel while other structural members use high strength steel (e.g., steel Q460 with the nominal yield strength of 460 MPa or steel Q690 with the nominal yield strength of 690 MPa). For this approach can result in reduced steel consumption and increased economic efficiency. Several finite element models of both HSS-EBFs and EBFs are established in this paper. Nonlinear hysteretic analyses and nonlinear time history analyses are conducted to compare seismic performance and economy of HSS-EBFs versus EBFs. Results indicate that the seismic performance of HSS-EBFs is slightly poorer than that of EBFs under the same design conditions, and HSS-EBFs satisfy seismic design codes and reduce material costs.

Keywords: high strength steel; eccentrically braced frames; seismic performance; finite element; nonlinear analysis

1. Introduction

Eccentrically braced frames (EBFs) have evolved from two existing lateral force resistant systems: moment-resisting frames (MRFs) and concentrically braced frames (CBFs). MRFs offer properties of ductility and energy dissipation at the expense of low stiffness. CBFs have high stiffness but lower energy dissipation capabilities. EBFs were developed to incorporate the best offered by MRFs and CBFs. Earthquake energy can be dissipated through plastic deformation of links in EBFs. Previous studies (Roeder and Popov 1978, Hjelmstad and Popov 1982, Foutch 1989, Bosco and Rossi 2009, Lin *et al*. 2010) have demonstrated that EBFs are reliable structural systems exhibiting satisfactory seismic performance. Improvements in the mechanical properties and weldability of high strength steel (HSS), along with the availability of improved welding consumables and welding processes, have allowed HSS to become an economical alternative to conventional steel. A previous study (Shi *et al*. 2011) indicates that Q460D structural steel, with nominal yield strength of 460 MPa, offers a useful combination of energy dissipation capability and ductility. At a time when HSS was being widely used in bridge structures (Miki *et al*. 2002,

*Corresponding author, Ph.D. Student, E-mail: lianming0821@163.com

Wasserman 2002, Azizinamini *et al*. 2004), it began to appear in building structure designs (Gresnigt and Steenhuis 1997, Yang and Hancock 2004, Tokgoz *et al*. 2012).

In eccentrically braced frames with high strength steel combination (HSS-EBFs), links use Q345 steel (specified nominal yield strength 345 MPa), braces use Q345 steel or HSS while other structural members use HSS (e.g., steel Q460 with the nominal yield strength of 460 MPa or steel Q690 with the nominal yield strength of 690 MPa). Slenderness ratio requirements for braces using conventional steel versus HSS may result in larger sections and increased material costs. As a point of reference, "conventional steel" is defined as steel with a specified nominal yield stress up to 345 MPa, whereas "HSS" is defined as steel with a specified nominal yield stress above 345 MPa. Typical HSS-EBFs and EBFs are shown in Fig. 1. Under earthquake loads, column, beam and brace members of HSS-EBFs are designed to remain in the elastic stage or have slight plastification while links enter the plastic stage completely. This structure can satisfy seismic design requirements with no demands of plastic deformation for the steel used in column and beam members. Under the same design conditions, considering the properties of HSS, HSS-EBFs have smaller member sections relative to EBFs. Therefore, HSS-EBFs offer seismic performance equivalent to that of EBFs and improved economy through reduced material costs. Currently, only four K shape HSS-EBFs specimens have been tested in Politehnica University of Timisoara in Romania (Dubina *et al*. 2008). These used removable links fastened to beams using flush end-plate bolted connections.

In the present study, the hysteretic behavior under cyclic loads is observed for one K-HSS-EBF specimen with a shear link. In order to study the seismic performance of HSS-EBFs and then compare it with that of EBFs, several K-HSS-EBFs and EBFs finite element models were established using the same design conditions and set up to conduct nonlinear hysteretic and time history analyses. On the basis of experimental and numerical results the economic efficiency of HSS-EBFs and EBFs are compared in terms of structural self-weight. Finally, some design suggestions of HSS-EBFs are given. However, the hysteretic pushover analyses may not provide accurate and reliable results because the distribution of the lateral loads is similar to that adopted in design and may differ from actual loads experienced during an earthquake. Structural deficiencies

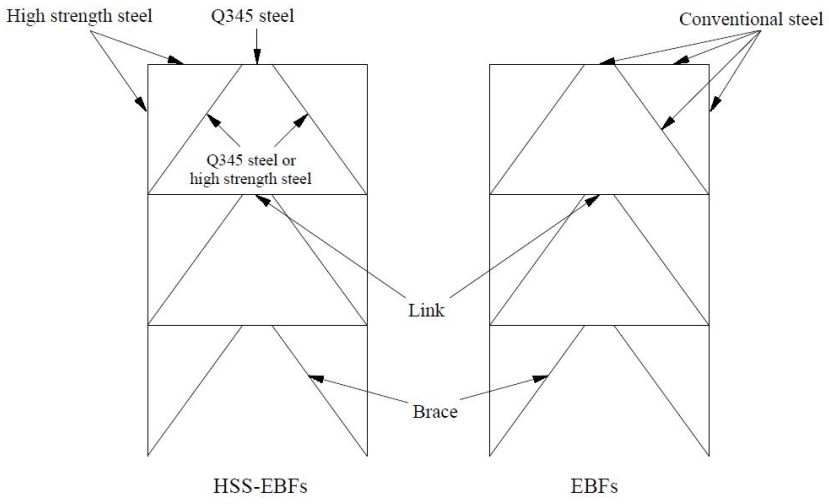

Fig. 1 HSS-EBFs and EBFs

may be hidden due to differences in lateral load distributions during hysteretic pushover analyses versus actual seismic events. Consequently, nonlinear dynamic analyses are conducted following the hysteretic pushover analyses.

2. Experimental description and finite element model of test

2.1 Experimental description

A 1:2 scale story and one-bay K-HSS-EBF specimen with a shear link was designed and manufactured for the experimental study of its hysteretic behavior. The story height and span of the specimen are 1.8 m and 3.6 m, respectively. The length of a shear link is 600 mm (eV_p/M_p = 1.45; where, e, M_p, and V_p are link length, the plastic shear capacity and the plastic moment capacity, respectively). Beams, columns and braces used steel Q460C with the nominal yield strength of 460 MPa while the link uses steel Q345B with the nominal yield strength of 345 MPa. Welded joints were used to connect link to beam and other elements in the test specimen. Furthermore, the link and beam had the same section in the specimen tested, but different sections can be adopted for link and beam members in practical engineering because the strength of the steel used in links is different from that in beams. Also, the links can be removed after an earthquake because the members using HSS remain in elastic stage by constraining plastic deformations to links. Full-depth web stiffeners are provided on both sides of the link web and the link is provided with intermediate web stiffeners with the transverse stiffeners of spacing 150mm. The detailed member sections are listed in Table 1, in which "H" refers to the welded H-shaped section, the following numbers are section depth h, flange width b_f, web thickness t_w and flange thickness t_f, respectively, with unit of mm (see Fig. 2). Mechanical properties of steel are presented in Table 2. The test setup is shown in Fig. 3.

A constant axial load of 800 kN with the axial compression ratio of 0.46 was applied by an oil jack pushing against the top of the column. The cyclic loading condition was generated by the

Table 1 Member sizes for the specimen

Member	Section
Beam	H225×125×6×10
Column	H150×150×6×10
Brace	H125×120×6×10
Link	H225×125×6×10

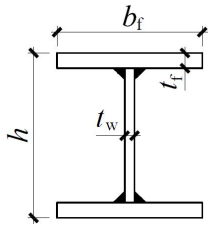

Fig. 2 Definition for the specimen sectional dimension

Table 2 Mechanical properties of steel

Steel	Thickness	Yield stress	Ultimate strength	Elastic modulus	Elongation ratio
	t (mm)	f_y (MPa)	f_u (MPa)	E ($\times 10^5$MPa)	(%)
Q345B	6	427.40	571.10	2.01	26.53
Q345B	10	383.33	554.40	2.00	31.03
Q460C	6	496.90	658.57	2.08	29.73
Q460C	10	468.77	627.97	2.02	35.88

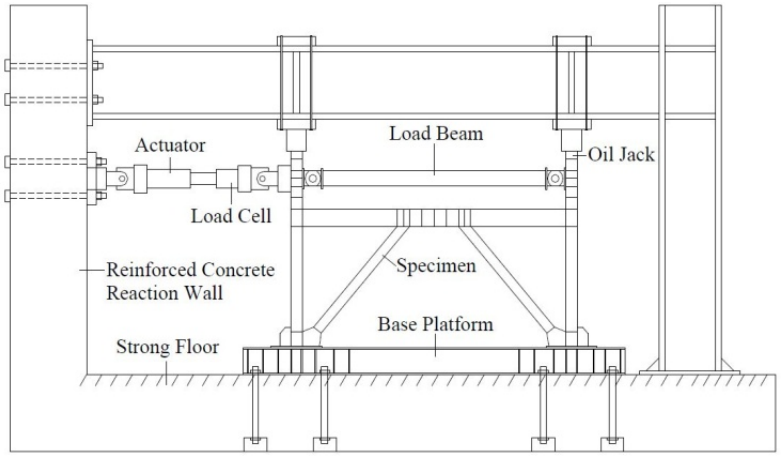

Fig. 3 Test setup

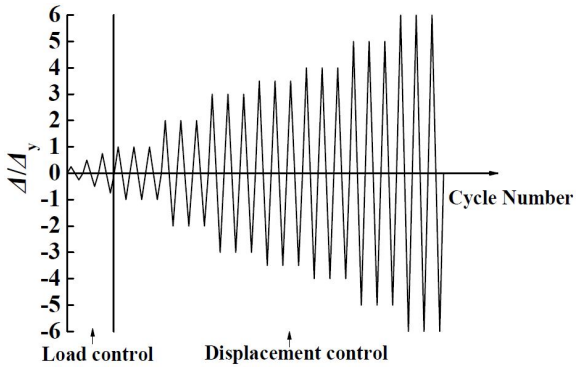

Fig. 4 Loading history

actuator that was connected to the specimen. The loading history is shown in Fig. 4. As seen from Fig. 4, the test loads began with a load control stage in which cyclic load reversals were applied until obvious stiffness degradation could be observed in the hysteretic curves of the specimen and the corresponding displacement was defined as the yield displacement (Δ_y). The following was displacement controlled. In this stage, the specimen was tested under displacement control for three cycles with the magnitude of $\pm\Delta_y$, $\pm2\Delta_y$, $\pm3\Delta_y$, $\pm3.5\Delta_y$ $\pm4\Delta_y$, $\pm5\Delta_y$, ….

Fig. 5 Failures of specimen

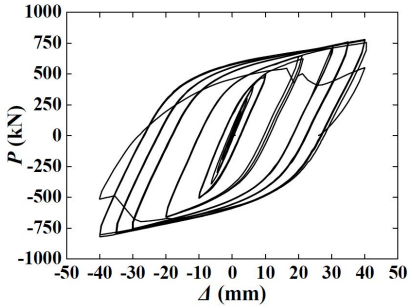

Fig. 6 Response curve

Table 3 Rotation and shear force of the link

Rotation (rad)		Shear force (kN)	
γ_m	$\gamma_{p,m}$	V_y	V_m
0.103	0.075	229	329.36

The link web near the stiffener weld and bottom flange weld tore when the displacement (Δ) at the intersection of beam and column equaled to 35.54 mm in the third cycle of $4\Delta_y$ (the yield displacement Δ_y of the specimen tested is 10.06 mm), and buckling occurred at the link web simultaneously. The link could not continue to resist loads and the test was stopped. The damage of the specimen is shown in Fig. 5. The maximum rotation γ_m, maximum plastic rotation $\gamma_{p,m}$, yield shear force V_y and the maximum shear force V_m of the link are shown in Table 3. The response curves of the specimen are shown in Fig. 6 and P is the force provided by actuator, which equals to the base shear force of the specimen. The curves show that the hysteretic loops are large and have no obvious deterioration in stiffness and load-carrying capacity within three cycles of same displacement. It can be inferred that the energy dissipation capacity of specimen is very significant.

2.2 Analytical models calibration and comparison of test

In order to better observe the behavior of shear links, solid elements were used for links that were meshed by using the software's "Structure" mesh type and beam elements were used for other members. Fig. 7 shows the experimental specimen and the finite element model in ABAQUS. Furthermore, the kinematic hardening material model and the Mises yield condition were adopted for the steel in the numerical model. Mechanical properties of steel used in the finite model are presented in Table 2.

Hysteretic curves and back-bone curves for both the test specimen introduced in this paper and the relevant finite element model are shown in Fig. 8. The analysis result has moderately good agreement with the experimental result, although the numerical result shows greater strength

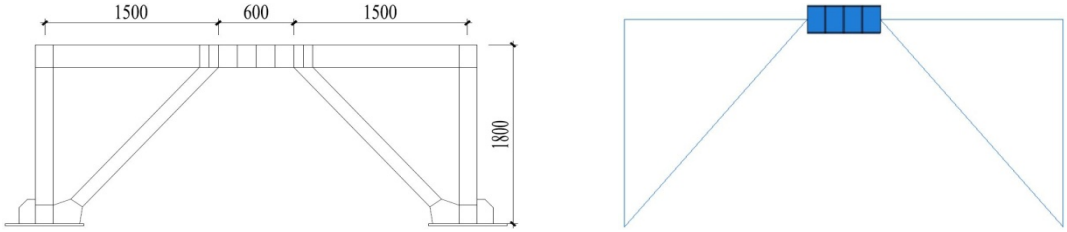

(a) Test specimen (b) Finite element model

Fig. 7 Experimental specimen and finite element model

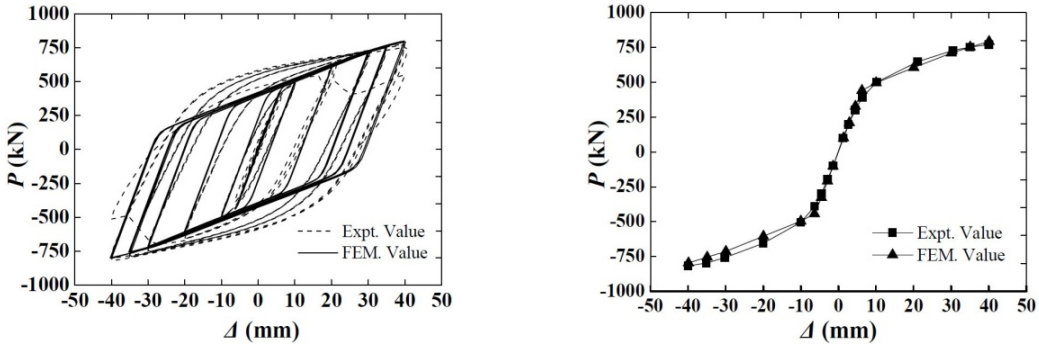

(a) Response curve comparison (b) Back-bone curve comparison

Fig. 8 Comparison of finite element analysis curves with experimental ones

Table 4 Results comparison

	Loading direction	Δ_y/mm	P_y/kN	Δ_u/mm	P_u/kN
Test	Positive direction	10.19	501.45	40.03	770.9
	Negative direction	10.03	505.64	39.97	817.55
Analysis	Positive direction	10.02	496.74	40.10	793.19
	Negative direction	9.97	496.35	39.89	796.43

during initial cycles with reduced values in subsequent cycles. Also, similar elastic and plastic behavior is observed between the test and the analysis. The analysis results of the model compared with the test are summarized in Table 4. The results show that both the model and the test have similar yield displacement Δ_y, yield load P_y, ultimate displacement Δ_u, and ultimate load P_u. The comparison between the finite element model and the test is carried out that the results of using ABAQUS for nonlinear analysis are available.

3. Finite element models

To investigate the seismic performance of K-HSS-EBFs, as compared with typical K-EBFs, several K-HSS-EBFs and K-EBFs were designed and analyzed.

3.1 Designs

Two groups of structure models were designed, four K-HSS-EBFs designs with shear links represented four building heights (eight, twelve, sixteen and twenty layers) were in group one, links and braces of structures used steel Q345 while other structural members used steel Q460 in this group (see Fig. 9); and four shear links K-EBFs prototypes with four building heights (eight, twelve, sixteen and twenty layers) were in group two and all members of K-EBFs used steel Q345 (see Fig. 9).

The designs are characterized by the peak ground acceleration of 0.3 g with 10% probability of exceedance in a 50-year period and moderately firm ground conditions. The factor that reduces the elastic response spectrum to obtain the design spectrum is 2.8 in GB50011-2010. The Alpha damping α and Beta damping β were specified according to the damping ζ and the fundamental frequencies of the structures. Moreover, the damping of 4% is considered for the steel building with the structural height not exceeding 50 m and 3% for structural heights between 50 and 200 m according to the requirements of GB50011-2010. In all designs, the story height is 3.6 m, there are five bays in the *x*-direction and three bays in the y-direction. The span in the x-direction is 7.2 m and that in the y-direction is 6 m (see Fig. 9). The constraints between columns of different stories were continuous and the rigid connections were used between columns and beams in all designs. Furthermore, the link had the same section of the beam connected at the same story. The frames located along the perimeter were designed to resist seismic loads and incorporated eccentric braces

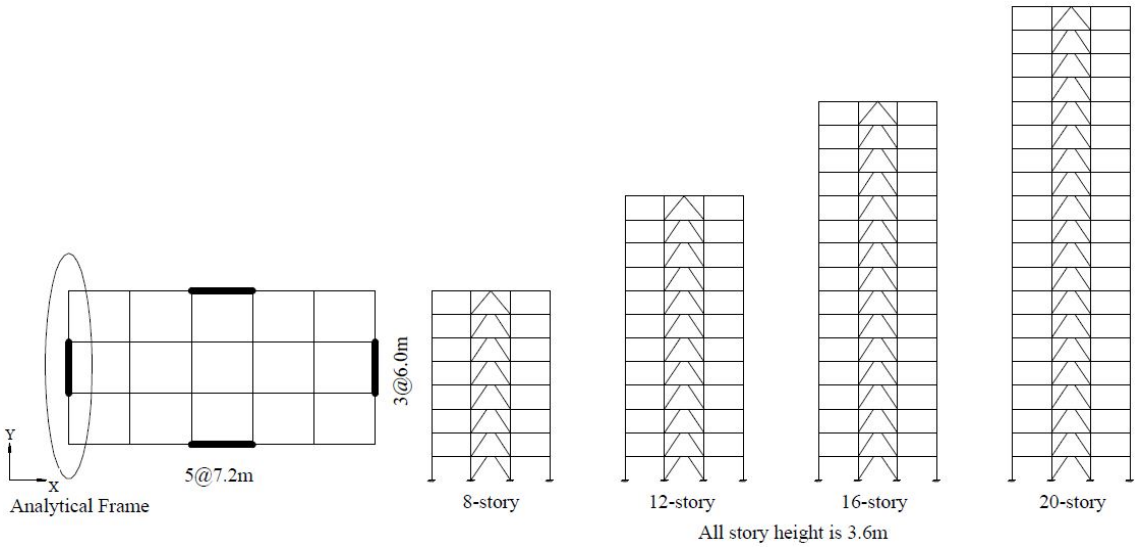

Fig. 9 Building plan and elevation views

Table 5 Natural periods for K-EBF and K-HSS-EBF designs

Structures	8-story		12-story		16-story		20-story	
	EBFs	HSS-EBFs	EBFs	HSS-EBFs	EBFs	HSS-EBFs	EBFs	HSS-EBFs
Natural period /s	1.002	1.108	1.393	1.556	2.004	2.168	2.208	2.389

Table 6 Member sizes of prototypes

Story	K-EBFs (8-story)				K-HSS-EBFs (8-story)			
	Central column	Edge column	Beam/Link	Brace	Central column	Edge column	Beam/Link	Brace
1-4	BOX 400×400×16	BOX 380×380×16	H400×300×14×20	H300×200×12×20	BOX 370×370×15	BOX 350×350×14	H350×250×14×20	H300×200×12×20
5-8	BOX 370×370×15	BOX 350×350×14	H350×250×14×20		BOX 320×320×13	BOX 320×320×12	H280×200×14×20	

Story	K-EBFs (12-story)				K-HSS-EBFs (12-story)			
	Central column	Edge column	Beam/Link	Brace	Central column	Edge column	Beam/Link	Brace
1-4	BOX 400×400×16	BOX 420×420×18	H400×300×14×20		BOX 380×380×16	BOX 350×350×16	H370×250×14×20	
5-8	BOX 360×360×15	BOX 380×380×16	H380×250×14×20	H300×200×12×20	BOX 350×350×16	BOX 330×330×13	H350×200×14×20	H300×200×12×20
9-12	BOX 340×3404×14	BOX 360×360×15	H350×250×14×20		BOX 320×320×13	BOX 300×300×12	H320×200×14×20	

Story	K-EBFs (16-story)				K-HSS-EBFs (16-story)			
	Central column	Edge column	Beam/Link	Brace	Central column	Edge column	Beam/Link	Brace
1-4	BOX 440×440×20	BOX 420×420×20	H480×350×14×25		BOX 420×420×20	BOX 390×390×18	H420×300×14×25	
5-8	BOX 420×420×20	BOX 410×410×20	H450×300×14×20		BOX 380×380×18	BOX 360×360×18	H380×300×14×25	
9-12	BOX 400×400×20	BOX 380×380×16	H400×300×14×20	H300×200×12×20	BOX 350×350×15	BOX 330×330×13	H350×280×14×25	H300×200×12×20
13-16	BOX 370×370×16	BOX 350×350×15	H380×250×14×20		BOX 320×320×13	BOX 300×300×12	H340×250×14×20	

Story	K-EBFs (20-story)				K-HSS-EBFs (20-story)			
	Central column	Edge column	Beam/Link	Brace	Central column	Edge column	Beam/link	Brace
1-4	BOX 530×530×25	BOX 500×500×24	H510×370×16×25		BOX 490×490×24	BOX 460×460×22	H490×350×16×30	
5-8	BOX 500×500×22	BOX 480×480×23	H500×350×14×25		BOX 450×450×22	BOX 430×430×22	H450×300×14×25	
9-12	BOX 480×480×20	BOX 450×450×22	H480×350×14×25	H400×300×14×20	BOX 420×420×20	BOX 400×400×20	H420×300×14×25	H350×300×14×20
13-16	BOX 440×440×20	BOX 410×410×18	H440×300×14×20		BOX 390×390×18	BOX 360×360×15	H400×300×14×25	
17-20	BOX 400×400×18	BOX 370×370×16	H400×300×14×20		BOX 360×360×15	BOX 330×330×14	H370×300×14×25	

Table 7 Link length and $e/(M_p/V_p)$ values

Story	Link length /mm and $e/(M_p/V_p)$							
	8-story		12-story		16-story		20-story	
	EBFs	HSS-EBFs	EBFs	HSS-EBFs	EBFs	HSS-EBFs	EBFs	HSS-EBFs
1-4	1100 (1.32)	750 (1.08)	1100 (1.32)	900 (1.28)	1400 (1.17)	1200 (1.18)	1400 (1.25)	1500 (1.21)
5-8	900 (1.29)	700 (1.26)	900 (1.28)	700 (1.22)	1100 (1.3)	1000 (1.28)	1400 (1.17)	1300 (1.26)
9-12			900 (1.29)	700 (1.24)	900 (1.08)	1000 (1.06)	1400 (1.17)	1200 (1.18)
13-16					900 (1.28)	900 (1.29)	1100 (1.30)	1200 (1.18)
17-20							1000 (1.32)	1200 (1.19)

Table 8 Designation of the models

Models	K-EBFs				K-HSS-EBFs			
	8-story	12-story	16-story	20-story	8-story	12-story	16-story	20-story
Designation	K-1	K-2	K-3	K-4	HK-1	HK-2	HK-3	HK-4

in the central span (see Fig. 9). However, as seen in Fig. 9, the frame is concentrically braced at the top story, because there will be no buckling in braces if they meet the strength requirements and seismic shear forces of top stories are low (JGJ 99-98). The dead load for the floors and roofs are 4.8 kN/m^2. The floor live load, roof live load and snow load use 2, 0.5 and 0.25 kN/m^2 respectively. Additionally, the HSS-EBFs mentioned in the previous section were designed to match the EBF story strengths rather than to use the equivalent lateral force procedure. Table 5 shows the fundamental natural period of each structure. The member sections and the link length (includes the length ratio $e/(M_p/V_p)$ of all designs) are summarized in Table 6 and Table 7, respectively. Furthermore, as seen in Table 6, "BOX" refers to the box section and the following numbers are section depth h, section width b and wall thickness t, respectively, with unit of mm. The designations of all models are summarized in Table 8.

ABAQUS was used for nonlinear analysis of all models. Solid elements were used for links that were meshed by using the software's "Structure" mesh type and beam elements were used for other structural members. Fig. 10 shows an 8-story finite element model used in ABAQUS. Nominal yield strength was adopted for steel materials, and the stress-strain response used the ideal elastic-plastic material model (Barth *et al*. 2000). The elastic modulus and Poisson's ratio are assumed to be 206,000 MPa and 0.3, respectively. In addition, nonlinear material behavior was modeled using the kinematic hardening rule and Von Mises yield criteria.

3.2 Loading history and boundary conditions

Models were subjected to lateral loads at all stories with an inverted triangular pattern for load distribution among the stories according to multiple point constraints. The loading history is shown in Fig. 11. In all models, beam-to-column connections were modeled as rigid joints and the column-to-base connections were assumed fully restrained. Also, the out-plane translational DOF of each beam was constrained in order to consider the impact of lateral supports, secondary beams and floors. Representative values of gravity equal to $1D + 0.5L$ are applied to the representative

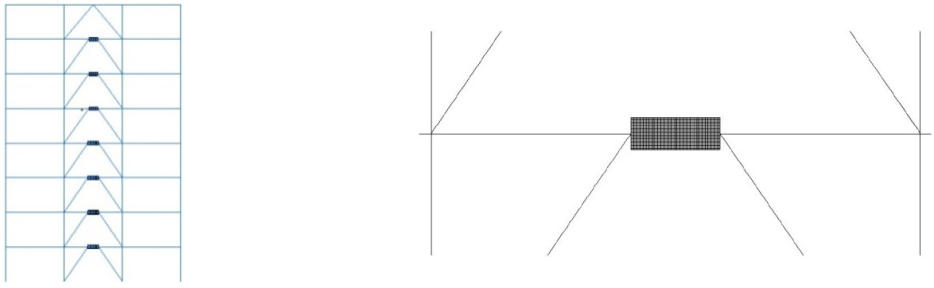

(a) (b)

Fig. 10 Finite element model

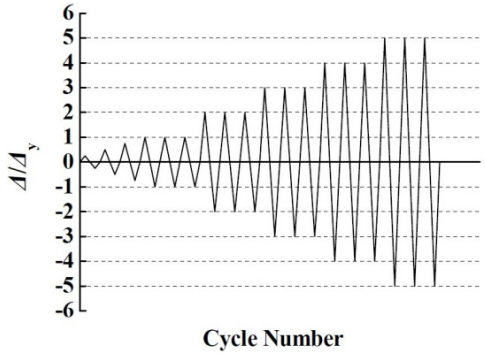

Fig. 11 Loading history

column, where D and L are dead load and live load, respectively. The influence of initial imperfections and residual stress is not considered and P-delta effects were included in the elastic and inelastic analyses.

4. Hysteretic analysis

The shear force-displacement curves of the models are illustrated in Fig. 12. All the models were loaded up to $4\Delta_y$ before the interstory displacement reached 5% of the story height (displacement of 180 mm) while K-1 and HK-1 reached $5\Delta_y$, where Δ_y is the yield displacement. Obviously, all the models possess stable and expanding hysteretic loops with no deterioration in stiffness and load-carrying capacity. Also, the hysteretic loops of each model are very plump and it can, therefore, be inferred that the energy dissipation capacity of both EBFs and HSS-EBFs is very significant.

The maximum plastic rotations in the links are presented in Table 9, which shows that the maximum plastic rotations in links have exceeded 0.08 rad. However, an interstory displacement equal to 5% may be too large for eccentrically braced structures, but the links using the steel with nominal yield strength of 345 MPa could reach the plastic deformations exceeding 0.08 rad (Okazaki and Engelhardt 2007) and all models had no load-carrying capacity deterioration when the interstory drift equaled to 5% (see Fig. 12). Because the finite element models do not consider

the fracture of metal and welds, no stiffness and strength degradation of the models appeared when the maximum interstory drift equaled to 5%. So the maximum interstory drift equaled to 5% of the story height was considered as criterion of structure failure for all models (Ellingwood 2001).

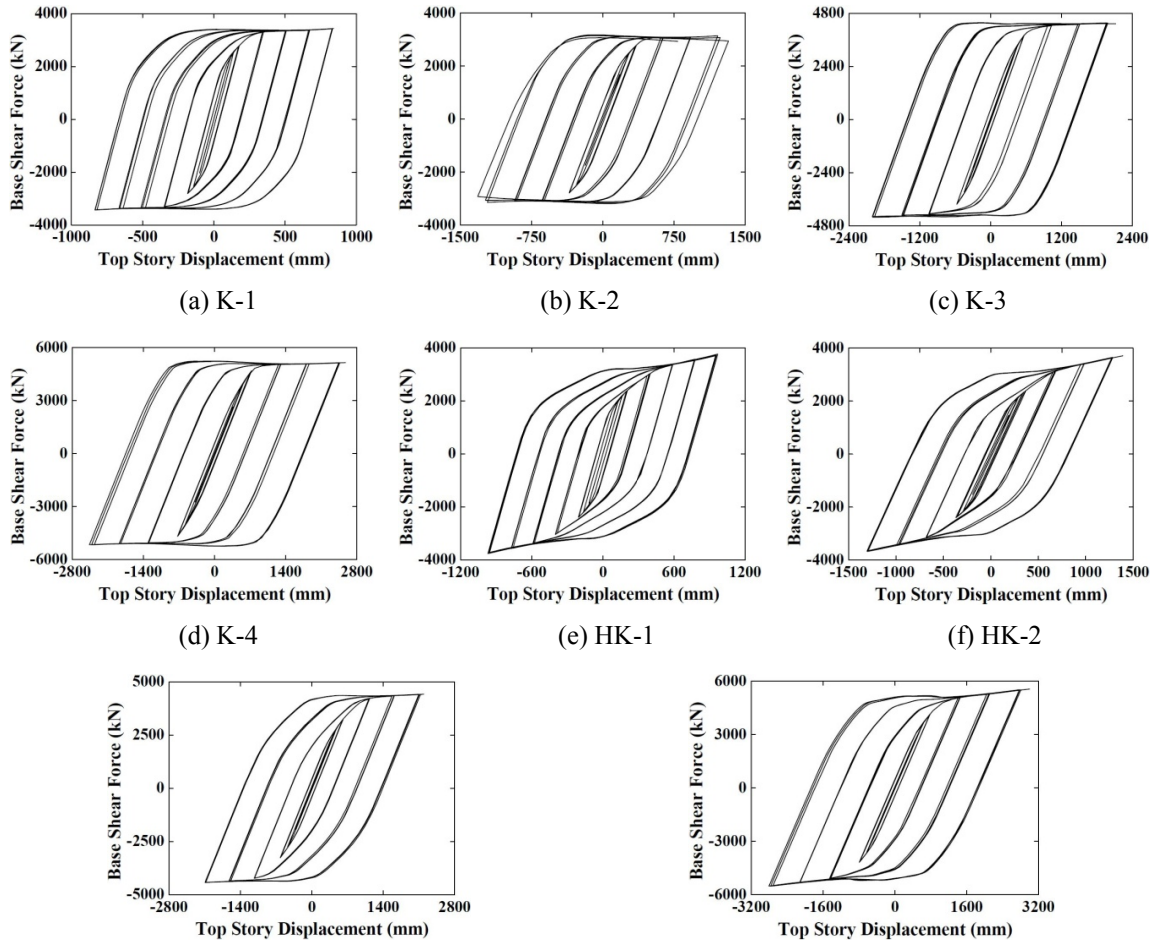

Fig. 12 Shear force-displacement curve of the models

Table 9 Maximum plastic rotations

Model name	K-1	HK-1	K-2	HK-2	K-3	HK-3	K-4	HK-4
Maximum plastic rotation (rad)	0.112	0.155	0.145	0.156	0.125	0.141	0.133	0.135

Table 10 Ultimate load-carrying capacity of the models

Model name	K-1	HK-1	K-2	HK-2	K-3	HK-3	K-4	HK-4
P (kN)	3427	3698	3147	3644	4361	4412	5140	5521

In order to study the hysteretic behavior of HSS-EBFs and compare the seismic performance with that of EBFs, the load-carrying capacity, stiffness, ductility, and energy dissipation capacity of all models will be discussed.

4.1 Load-carrying capacity

The load-carrying capacity keeps increasing prior to failure (refer to Fig. 12). Hence, the value of the base shear is used when the maximum interstory displacements equal to 5% of the story height (displacement of 180 mm) for the ultimate load-carrying capacity of the model. The value of the ultimate load-carrying capacity of the models is presented in Table 10. The data indicate that the HSS-EBFs models reach a larger load-carrying capacity compared with the EBF models with the same number of stories although the HSS-EBF models have smaller member sizes. The load value of model HK-1 is 8% higher than that of model K-1. For models HK-2, HK-3, and HK-4 compared with models K-2, K-3 and K-4, the differences are 16%, 1.2% and 7%, respectively. Analysis results indicate that, under the same design conditions, HSS-EBFs can satisfy load-carrying requirements while using smaller member sizes relative to EBFs.

4.2 Stiffness degradation

Model back-bone curves are presented in Fig. 13. They indicate no deterioration in load-carrying capacity at large placement stages. As seen in the back-bone curves, the yield base shear force of EBF models is larger than that of the HSS-EBF models, while the maximum base shear force of EBF models is smaller in the later cycles.

Stiffness of all the models could be calculated as

$$K = \frac{\left|P^{+}\right| + \left|P^{-}\right|}{\left|\Delta^{+}\right| + \left|\Delta^{-}\right|} \tag{1}$$

where P^{+} and P^{-} are the maximum lateral force in the positive and negative directions in the same hysteretic loop; and Δ^{+} and Δ^{-} are the maximum top story displacement in the positive and negative directions in the same hysteretic loop of P^{+} and P^{-}. The stiffness degradation could reflect the stiffness variation of models during the loading cycles. Fig. 14 shows the stiffness degradation curves of the models given by Eq. (1). The curves show that the stiffness which is under the yield load of the models in group one is higher than that of models in group two, and this phenomenon dues to the smaller member sections of HSS-EBF models, leading lower lateral stiffness compared with the EBF models. The stiffness under the yield load of model HK-1 is 24% lower than that of model K-1. For models HK-2, HK-3 and HK-4 compared with models K-2, K-3 and K-4, the differences are 21%, 20% and 17%, respectively. However, the stiffness of EBFs models has a noticeable decrease. This is more evident than that of HSS-EBFs models during the subsequent loading cycles. The performance of EBFs is influenced more obviously than that of HSS-EBFs by cumulative damages. The stiffness which is under the yield load of HSS-EBFs is lower than that of EBFs. This presents a less obvious decrease of stiffness at a large displacement stage.

4.3 Ductility capacity

The displacement ductility coefficient of all the models could be calculated as

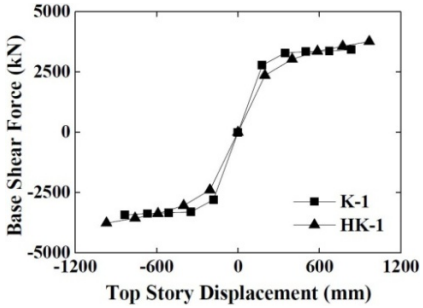

(a) 8-story models

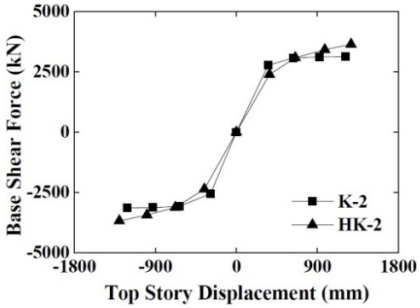

(b) 12-story models

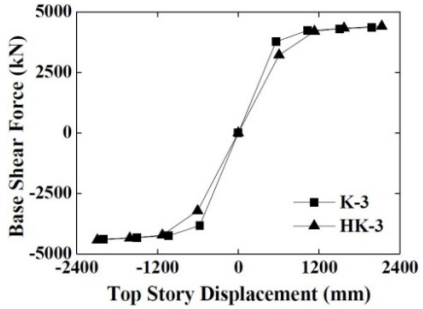

(c) 16-story models

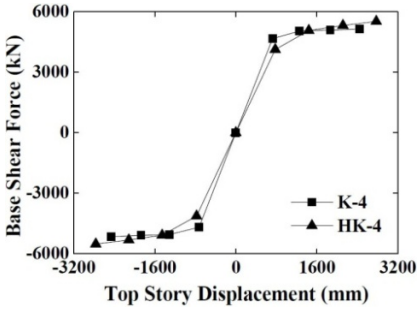

(d) 20-story model

Fig. 13 Back-bone curves

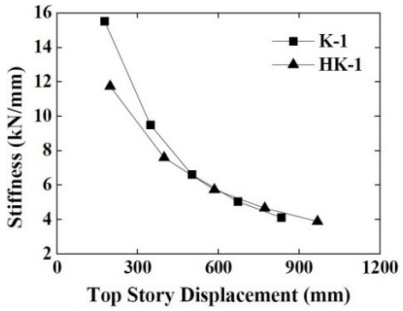

(a) 8-story models

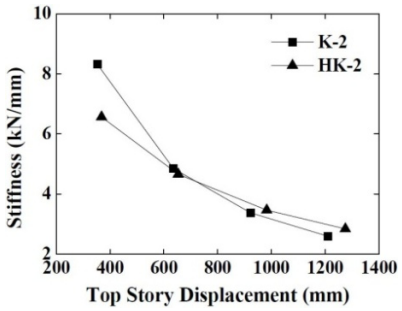

(b) 12-story models

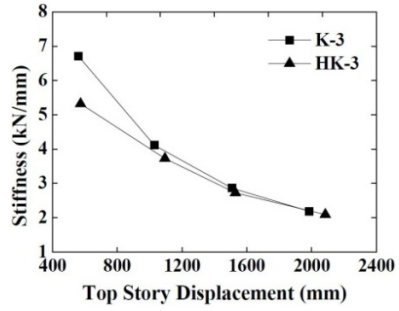

(c) 16-story models

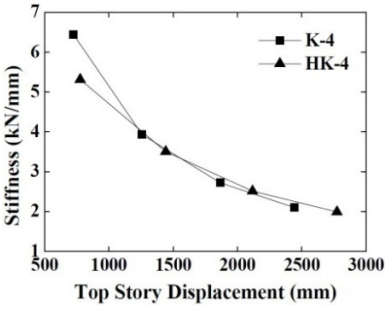

(d) 20-story model

Fig. 14 Stiffness degradation curves

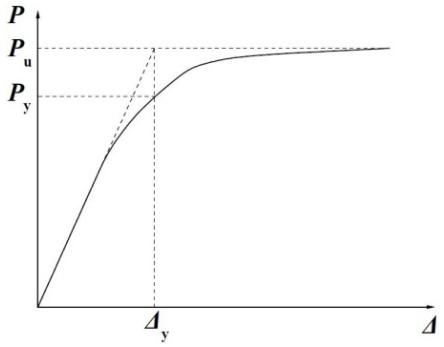

Fig. 15 The method based on equivalent elastic-plastic yield

Table 11 Displacement ductility coefficients of the models

Model name	Δ_y/mm	Δ_y/H	Δ_u/mm	Δ_u/H	μ
K-1	153	1/188	834	1/35	5.45
K-2	300	1/144	1325	1/33	4.42
K-3	525	1/110	2120	1/27	4.04
K-4	655	1/110	2580	1/28	3.94
HK-1	170	1/171	963	1/30	5.66
HK-2	343	1/126	1392	1/31	4.06
HK-3	586	1/98	2197	1/26	3.75
HK-4	778	1/93	2774	1/26	3.57

$$\mu = \frac{\Delta_u}{\Delta_y} \tag{2}$$

where Δ_u and Δ_y are the ultimate displacement and yield displacement. The Δ_y of each structure was determined based on the method that is shown in Fig. 15 (Park 1988).

Because there is no deterioration in load-carrying capacity along with the increasing of displacement (refer to Fig. 12), the ultimate placement Δ_u employed the maximum interstory displacement equaled to 5% of the story height. The top story displacements, global drifts and displacement ductility coefficients of the models are summarized in Table 11 and H is the height of the models. Except model K-1, the displacement ductility coefficient of EBF models is slightly higher than that of HSS-EBF models with the same number of stories, which shows that the ductility capacity of HSS-EBFs is slightly lower than that of EBFs. However, the displacement ductility coefficient of each model is about 4, showing good ductility of both HSS-EBFs and EBFs. The overall drift of models in group two is higher than that of models in group one because of the smaller member sizes of HSS-EBFs, leading lower overall stiffness of HSS-EBFs compared with EBFs. Finally, it is concluded that the ductility of EBFs is slightly better than that of HSS-EBFs.

4.4 Energy dissipation capacity

As seen in Fig. 16, the total dissipated energy values of the models are presented, where the

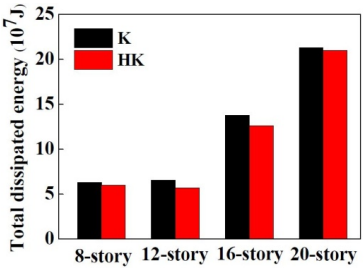

Fig. 16 Total dissipated energy values of the models

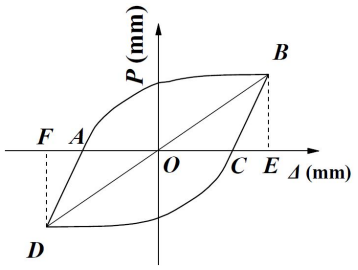

Fig. 17 Calculation of energy dissipation coefficient

dissipated energy values of EBF models are slightly higher than those of HSS-EBF models. The dissipated energy value of model K-1 is 5% higher than that of model HK-1. For models K-2, K-3, and K-4 compared with models HK-2, HK-3, and HK-4, the differences are 15%, 9% and 1.4%, respectively.

The energy dissipation coefficient E could be calculated as

$$E = \frac{S_{ABC} + S_{CDA}}{S_{OBE} + S_{ODF}} \tag{3}$$

S_{ABC}, S_{CDA}, S_{OBE}, S_{ODF} are shown in Fig. 17. In Table 12, the energy dissipation coefficients of the models are presented. The energy dissipation coefficient increases steadily after the links begin to yield, which indicates that the energy dissipation capacity of all models keeps on increasing with the increase of displacement. Except model HK-2, the energy dissipation coefficient of HSS-EBF models is higher than that of EBF models with the same number of stories under the displacement of $1\Delta_y$, which illustrates that the energy dissipation capacity of HSS-EBFs is better than that of EBFs in the first cycle. However, the energy dissipation coefficient of HSS-EBF models increases more slowly than that of EBF models and the maximum energy dissipation coefficient of HSS-EBF models is lower than that of EBF models. The maximum value of the energy dissipation coefficient of HSS-EBFs ranges from 2.1082 to 2.4329 while the maximum value of the energy dissipation coefficient of EBFs ranges from 2.691 to 3.6367, which indicates that the energy dissipation capacity of both HSS-EBFs and EBFs are excellent, but the energy dissipation capacity of HSS-EBFs is slightly lower than that of EBFs.

Table 12 Energy dissipation coefficient of the models

Displacement (mm)	Energy dissipation coefficient							
	K-1	K-2	K-3	K-4	HK-1	HK-2	HK-3	HK-4
$1\Delta y$	0.8057	0.5300	0.3479	0.3184	0.8842	0.4132	0.3812	0.3397
$2\Delta y$	1.7213	1.7703	1.5530	3.4722	1.4237	1.2171	1.1530	1.3194
$3\Delta y$	2.3933	2.4379	2.2897	3.5696	1.8840	1.7264	1.9606	1.9933
$4\Delta y$	2.6910	2.8587	2.7029	3.6367	2.2520	2.1082	2.3437	2.4329
$5\Delta y$	2.9585				2.3701			

5. Time history analysis

5.1 Ground motion records

In order to study the deformation performance of the HSS-EBFs during earthquakes compared with that of EBFs, all models were subjected to nonlinear time history analyses with various ground motions. Dynamic analyses were performed using suites of ten earthquake records and the seismological properties of the records are summarized in Table 13, which also shows that three levels of seismic hazard were employed: 50%, 10% and 2% probability of exceedance in a 50-year period. The hypocentral distances from the sources for the earthquake records range between 1.0 km (Kobe, in Japan) and 43.4 km (Chi-Chi, in Taiwan). Therefore, the above suite of strong motions covers well-defined design scenarios, i.e., near and far-field conditions. The acceleration response spectra of the ensemble of accelerograms, along with the design acceleration spectrum are shown in Fig. 18.

Three structural performance levels, i.e., immediate occupancy, life safety and collapse prevention limit states, are considered for the system assessment carried out in the present study. These limit states are in compliance with seismic suggestions by FEMA 356. The relationship between overall seismic performance and maximum transient drift ratios are summarized in Table

Table 13 Characteristics of ground motions

Earthquake	Record	Pr. of exc. (% in 50 yrs)	Magnitude	Source distance (km)	PGA (g)	PGV (cm/s)	Scale factors
Imperial Valley	117 El Centro Array #9, IMPVALL/I-ELC180	50/10/2	7	8.3	0.313	29.8	0.35/0.96/1.63
Kern County	1095 Taft Lincoln School, KERN/TAF021	50/10/2	7.4	41	0.156	15.3	0.71/1.92/3.27
Chi-Chi, Taiwan	TCU095, ChiChi/TCU095-W	50/10/2	7.6	43.4	0.379	62	0.29/0.79/1.35
Northridge	24278 Castaic - Old Ridge Route, NORTHR/ORR090	50/10/2	6.7	20.1	0.568	52.1	0.19/0.53/0.90
Friuli, Italy	8012 Tolmezzo, FRIULI/A-TMZ270	50/10/2	6.5	15.5	0.315	30.8	0.35/0.95/1.62
Loma Prieta	47006 Gilroy - Gavilan Coll, LOMAP/GIL067	50/10/2	6.9	10	0.357	28.6	0.31/0.84/1.43
Cape Mendocino	89324 Rio Dell Overpass - FF, CAPEMEND/RIO360	50/10/2	7	14.3	0.549	42.1	0.20/0.55/0.93
Landers	22170 Joshua Tree, LANDERS/JOS000	50/10/2	7.3	11	0.274	27.5	0.40/1.10/1.86
Kobe Japan	0 KJMA, KOBE/KJM090	50/10/2	6.9	1	0.599	74.3	0.18/0.50/0.85
Superstitn Hills	01335 El Centro Imp. Co. Cent, SUPERST/B-SUP135	50/10/2	6.5	5.6	0.894	42.2	0.12/0.34/0.57

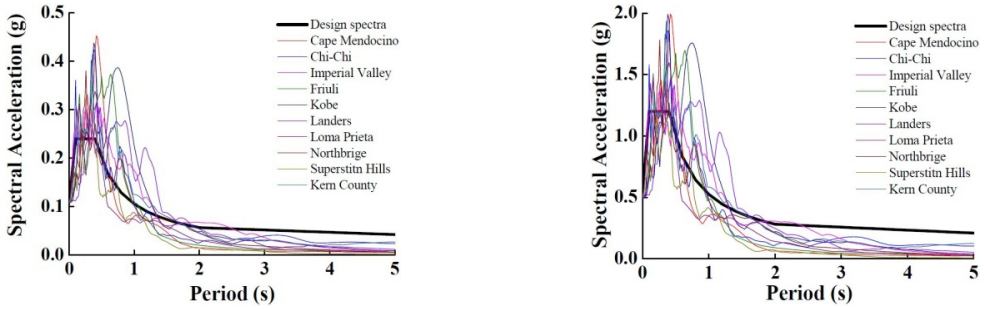

(a) Spectra comparison of earthquakes with 50% pr. of exc. in 50 years

(b) Spectra comparison of earthquakes with 2% pr. of exc. in 50 years

Fig. 18 Design spectra and scaled earthquake spectra

Table 14 Limit states and drift limits (FEMA 356)

Performance level	Qualitative description	Recommended drifts (i.e., EBF systems) (%)
SP-1	Immediate occupancy	0.5
SP-2	Life safety	1.5
SP-3	Collapse prevention	2.0

14. Three deformational quantities are monitored herein, namely interstory drifts (d/h, where d and h are interstory displacements and height of the story, respectively), roof drifts (D/H, where D and H are the top displacements and total height of the models, respectively) and maximum plastic rotations of links. The former are primary global performance parameters, while the plastic rotations measure link performance. The results of the dynamic analyses are discussed hereafter.

5.2 Global deformations

The mean maximum interstory drifts (d/h) for the EBFs and HSS-EBFs were found for the earthquakes with probability exceedance of 50% as displayed in Fig. 19. The mean maximum interstory drifts for both EBFs and HSS-EBFs are smaller than the "immediate occupancy" limit (0. 5%), and the estimated values are 0.35% (K-1) and 0.39% (HK-1), 0.35% (K-2) and 0.40%

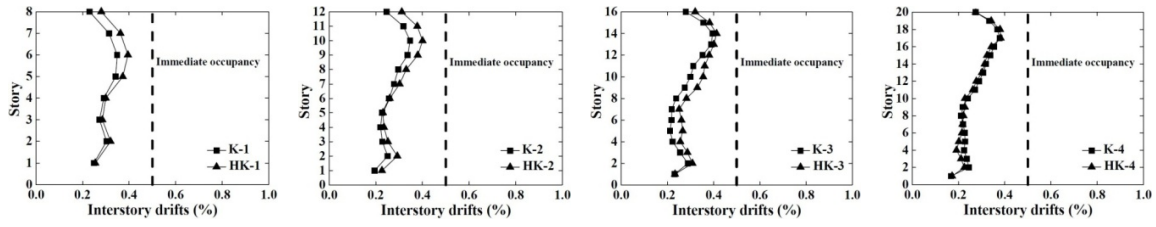

(a) 8-story models (b) 12-story models (c) 16-story models (d) 20-story model

Fig. 19 Mean maximum interstory drifts of models during the earthquakes with 50% pr. of exc.

(HK-2), 0.40% (K-3) and 0.41% (HK-3), 0.37% (K-4) and 0.38% (HK-4). The mean maximum interstory drifts of HSS-EBFs are slight larger than those of EBFs besides several stories in the 20-story models. This is because the member sections of HSS-EBFs are smaller than those of EBFs, leading lower lateral stiffness and larger interstory drifts.

For the serviceability check, as seen in Fig. 19, the interstory drifts of HSS-EBF models are larger than those of EBF models, indicating that the HSS-EBF models have lower lateral stiffness caused by the smaller member sections than EBF models do. However, all models have interstory drifts less than the limitation of "immediate occupancy" though the drifts of HSS-EBF models are larger than those of EBF models, indicating that both of HSS-EBFs and EBFs models have good capacity in controlling story drifts.

The results summarized in Table 15 show the mean maximum roof drift (D/H) of models during the earthquakes with probability exceedance of 50%. The roof lateral drift of HSS-EBFs is larger than that of EBFs. The value of model HK-1 is 3.5% higher than that of model K-1, for models HK-2, HK-3, and HK-4 compared with models K-2, K-3 and K-4, the differences are 3.2%, 14% and 8.9%, respectively. The increment of the lateral deformations due to the smaller member sections of HSS-EBFs result in lower lateral stiffness than that of EBFs.

For earthquakes with probability exceedance of 10%, the mean maximum interstory drifts (d/h) for the EBFs and HSS-EBFs are shown in Fig. 20. Most of the mean maximum interstory drifts for both EBFs and HSS-EBFs are between the "immediate occupancy" limit (0.5%) and "life safety" limit (1.5%). It is found that EBFs exhibit lower than HSS-EBFs (less than 12%).

Table 16 shows the mean maximum roof drift (D/H) of models during the earthquakes with probability exceedance of 10%. The roof lateral drift of EBFs is smaller than that of HSS-EBFs. The value of model K-1 is 4.4% higher than that of model K-1, for models K-2, K-3, and K-4 compared with models HK-2, HK-3 and HK-4, the differences are 7.5%, 3.9% and 6.2%, respectively.

Table 15 Mean maximum roof drift of models during the earthquakes with 50% pr. of exc.

Model name	K-1	HK-1	K-2	HK-2	K-3	HK-3	K-4	HK-4
Roof drift (%)	0.234	0.241	0.188	0.193	0.160	0.183	0.151	0.164

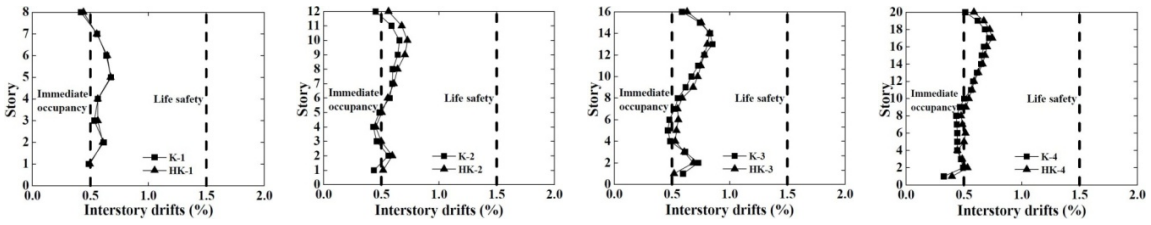

(a) 8-story models (b) 12-story models (c) 16-story models (d) 20-story model

Fig. 20 Mean maximum interstory drifts of models during the earthquakes with 10% pr. of exc.

Table 16 Mean maximum roof drift of models during the earthquakes with 10% pr. of exc.

Model name	K-1	HK-1	K-2	HK-2	K-3	HK-3	K-4	HK-4
Roof drift (%)	0.456	0.458	0.372	0.402	0.366	0.381	0.317	0.338

The mean maximum interstory drifts (d/h) of models during the earthquakes with probability exceedance of 2% are shown in Fig. 21, which shows that the interstory drifts of all models arebelow the "Collapse prevention" limit (2%) in all cases. Both of EBFs and HSS-EBFs are effective for high-magnitude earthquakes and hence in the inelastic range. The interstory drifts in those in EBFs, indicating that the deformation capacity of HSS-EBFs is close to that of EBFs during the earthquakes with probability exceedance of 2%, though the member sections of HSS-EBFs are smaller than those of EBFs.

The results shown in Table 17 are the mean maximum roof drift (D/H) of models during the earthquakes with probability exceedance of 2%. HSS-EBFs have higher roof lateral drift than EBFs. The value of model HK-1 is 6.2% higher than that of model K-1, for models HK-2, HK-3, and HK-4 compared with models K-2, K-3 and K-4, the differences are 6.1%, 7.2% and 6.9%, respectively.

5.3 Plastic rotations of links

The links of both EBFs and HSS-EBFs remained in elastic stage during the earthquakes with probability exceedance of 50%. The mean maximum plastic rotations of links in EBFs and HSS-EBFs during the earthquakes with probability exceedance of 10% and 2% are summarized in Table 18 and Table 19, respectively. The rotations of links HSS-EBFs show greater plastic rotation

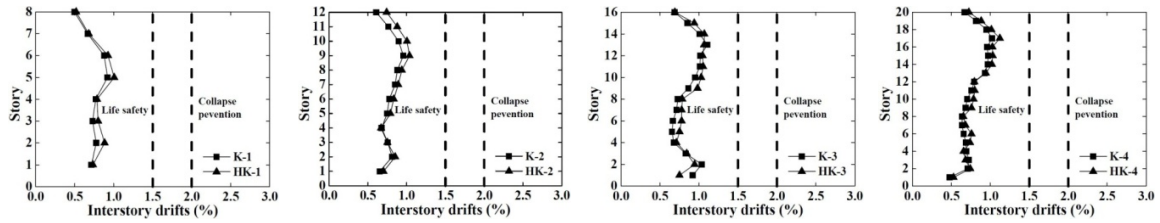

(a) 8-story models (b) 12-story models (c) 16-story models (d) 20-story model

Fig. 21 Mean maximum interstory drifts of models during the earthquakes with 2% pr. of exc.

Table 17 Mean maximum roof drift of models during the earthquakes with 2% pr. of exc.

Model name	K-1	HK-1	K-2	HK-2	K-3	HK-3	K-4	HK-4
Roof drift (%)	0.58	0.616	0.573	0.608	0.501	0.537	0.465	0.497

Table 18 Mean maximum plastic rotation of links during the earthquakes with 10% pr. of exc.

Model name	K-1	HK-1	K-2	HK-2	K-3	HK-3	K-4	HK-4
Plastic rotation (rad)	0.0135	0.0243	0.0140	0.0218	0.0124	0.0203	0.0089	0.0098

Table 19 Mean maximum plastic rotation of links during the earthquakes with 2% pr. of exc.

Model name	K-1	HK-1	K-2	HK-2	K-3	HK-3	K-4	HK-4
Plastic rotation (rad)	0.0198	0.0363	0.0230	0.0349	0.0191	0.0301	0.0139	0.0159

of links than EBFs in all cases, the increments of plastic rotation of the former is more than 50% than the latter. It indicates that the smaller member sections and lower lateral stiffness of HSS-EBFs result in the larger interstory displacements and plastic rotations of links than those in EBFs during the high-magnitude earthquakes.

In conclusion, the results of nonlinear pushover and dynamic analyses indicate that the main reason why EBFs and HSS-EBFs do not have the same seismic performance is that the application of HSS to beam and column members results in smaller sections which reduce the lateral stiffness of the building structure. As the building heights increase, the drift demands increase and HSS-EBFs do not perform as effectively as EBFs.

6. The advantages of HSS-EBFs compared with EBFs

The steel weight of eight prototypes of EBFs and HSS-EBFs are listed in Table 20 and Fig. 22. In Table 20, ratio = $(m_1 - m_2) / m_1$, where m_1 and m_2 are the weight of EBF and HSS-EBF models, respectively. They indicate that HSS-EBF designs are lighter than EBF designs with the same architectural function. The 8-story HSS-EBF design weights 23% less than the corresponding EBF design. For the 12, 16, and 20-story designs, the weight decrease ratios of HSS-EBFs relative to EBFs are 16%, 12% and 7%, respectively. Note that, as structural height increases, weight differences between HSS-EBF and EBF designs gradually decrease. HSS-EBF designs use HSS, which results in smaller member sections than those of the EBF designs using conventional steel. However, as the structural height increases, the lateral stiffness requirements are more considerable, which reduces the advantage of saving steel using HSS-EBFs. Based on the analyses described in this paper, HSS-EBFs perform best when building heights do not exceed sixteen stories.

The strength of columns fabricated from HSS have higher strength than that of the columns of equal length and cross-section fabricated from conventional steel when compared on a nondimensional basis, which because the ratios of residual stress at critical points in the cross-section to the yield stress are less for HSS columns than for conventional steel columns, and the ratio of residual stress to the yield stress, rather than the magnitude of residual stress itself, which governs the reduction in strength (Rasmussen and Hancock 1992, 1995). The ratio is lower for HSS because the magnitude of residual stress is largely independent of the yield stress. It can use a higher value of the slenderness reduction factor for columns used HSS than the value

Table 20 Weight of the prototypes

Prototype	Weight (t)	Ratio (%)
8-story HSS-EBF design	242	23%
8-story EBF design	314	
12-story HSS-EBF design	468	16%
12-story EBF design	559	
16-story HSS-EBF design	820	12%
16-story EBF design	929	
20-story HSS-EBF design	1312	7%
20-story EBF design	1418	

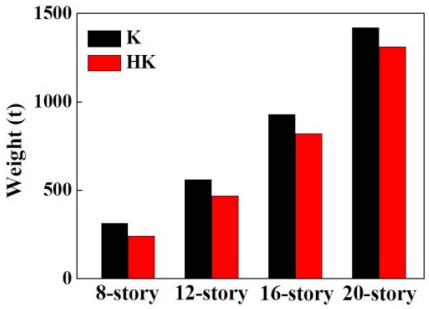

Fig. 22 Weight comparison

adopted for columns used from ordinary steel (Ban *et al*. 2011), so that the influence of residualstress on the strength of high strength steel columns is reduced in design. For low-cycle fatigue, where the stress range is higher and where the strain range is the governing load, HSS has an advantage over conventional steel (Vander *et al*. 1990). The application of HSS to beam and column members of HSS-EBFs can reduce the member sections and structure weight which can reduce the damage of the earthquakes to structures (Pocock 2006). In addition, modern HSS can be safe in using, because of its good weldability and resistance against brittle fracture. Moreover, it can lead to considerable savings in steel consumption of welding and retardant paint (e.g., fire retardant paint and rust preventing paint) which is the most impact on cost. When HSS is used, the amount of welding is reduced because the smaller plate thicknesses and the smaller size of the actual weld throat thickness can improve the quality of welding and the fatigue life of structure members. Additionally, as compared with the EBFs, HSS-EBFs can provide more areas to be used in the building because of the smaller section of structure members.

7. Conclusions

Seismic performance and economy of eccentrically braced frames with HSS combination (HSS-EBFs) are compared with traditional EBFs in this paper. Four HSS-EBFs are designed with story strengths similar to those of the four EBFs. The finite element models of HSS-EBFs and EBFs are analyzed under the cyclic loading and dynamic loading using three ground motions and the seismic performance of each model is verified by comparisons.

The following conclusions can be made on the basis of this study:

- HSS-EBFs have a better loading-carry capacity than that of EBFs.
- The lateral stiffness of HSS-EBFs is lower than that of EBFs.
- The ductility capacity of both HSS-EBFs and EBFs is good, but EBFs have a slight advantage.
- The energy dissipation capacity of both HSS-EBFs and EBFs is good, but HSS-EBFs have a slightly lower energy dissipation capacity than that of EBFs.
- The maximum story drifts, roof drift and maximum plastic rotation of links in HSS-EBFs are greater than those in EBFs under dynamic loading.
- HSS-EBFs are lighter than EBFs, leading to reduced material costs.
- HSS-EBF systems perform best when structure height does not exceed sixteen stories.

Acknowledgments

The authors are grateful for the financial support from the National Natural Science Foundation of China (Grant No. 51178382). Thanks also go to Prof. H. Zhu and Mike Brewes of Nipissing University, Canada for their assistance in proofreading this article.

References

Azizinamini, A., Barth, K., Dexter, R. and Rubeiz, C. (2004), "High performance steel: Research front – historical account of research activities", *J. Bridge Eng.*, **9**(3), 212-217.

Ban, H.Y., Shi, G., Liu, Z., Shi, Y., Want, Y., Xing, H. and Li, M. (2011), "Experimental study on overall buckling behavior of Q420 high strength equal angle members under axial compression", *J. Build. Struct.*, **32**(2), 60-67.

Barth, K.E., White, D.W. and Bobb, B.M. (2000), "Negative bending resistance of HPS70W girders", *J. Construct. Steel Res.*, **53**(1), 1-31.

Bosco, M. and Rossi, P.P. (2009), "Seismic behaviour of eccentrically braced frames", *Eng. Struct.*, **31**(3), 664-674.

Dubina, D., Stratan, A. and Dinu, F. (2008), "Dual high-strength steel eccentrically braced frames with removable links", *Earthq. Eng. Struct. Dyn.*, **37**(15), 1703-1720.

Ellingwood, B.R. (2001), "Earthquake risk assessment of building structures", *Reliab. Eng. Syst. Safe.*, **74**(3), 251-262.

FEMA 356 (2000), Prestandard and Commentary for the Seismic Rehabilitation of Buildings; Washington, D.C., USA.

Foutch, D.A. (1989), "Seismic behavior of eccentrically braced steel building", *J. Struct. Eng.*, **115**(8), 1857-1876.

GB50011-2010 (2010), Code for Seismic Design of Buildings; Beijing, China.

Gresnight, A.M. and Steenhuis, C.M. (1997), "High strength steels", *Progress in Structural Engineering and Materials*, **1**(1), 31-41.

Hjelmstad, K.D. and Popov, E.P. (1982), "Characteristics of eccentrically braced frames", *J. Struct. Eng.*, **110**(2), 340-353.

JGJ 99-98 (1998), Technical Specification for Steel Structure of Tall Buildings; Beijing, China.

Lin, K.C., Lin, C.C.J., Chen, J.Y. and Chang, H.Y. (2010), "Seismic reliability of steel framed buildings", *Struct. Safe.*, **32**(3), 174-182.

Miki, C., Homma, K. and Tominaga, T. (2002), "High strength and high performance steels and their use in bridge structures", *J. Construct. Steel Res.*, **58**(1), 3-20.

Okazaki, T. and Engelhardt, M.D. (2007), "Cyclic loading behavior of EBF links constructed of ASTM A992 steel", *J. Construct. Steel Res.*, **63**(6), 751-765.

Park, R. (1988), "Ductility evaluation from laboratory and analytical testing", *Proceedings of the 9th World Conference on Earthquake Engineering*, Tokyo, Japan, August, pp. 605-616.

Pocock, G. (2006), "High strength steel use in Australia, Japan and the US", *The Struct. Eng.*, **84**(21), 27-30.

Rasmussen, K.J.R. and Hancock, G.J. (1992), "Plate slenderness limits for high strength steel sections", *J. Construct. Steel Res.*, **23**(1), 73-96.

Rasmussen, K.J.R. and Hancock, G.J. (1995), "Tests of high strength steel columns", *J. Construct. Steel Res.*, **34**(1), 27-52.

Roeder, C.W. and Popov, E.P. (1978), "Eccentrically braced steel frames for earthquake", *J. Struct. Div.*, **104**(3), 391-412.

Shi, G., Wang, M., Bai, Y., Wang, F., Shi, Y. and Wang, Y. (2011), "Experimental and modeling study of high-strength structural steel under cyclic loading", *Eng. Struct.*, **37**(5), 1-13.

Tokgoz, S., Dundar, C. and Tanrikulu, A.K. (2012), "Experimental behaviour of steel fiber high strength

reinforced concrete and composite columns", *J. Construct. Steel Res.*, **74**(7), 98-107.
Wasserman, E.P. (2002), "Optimization of HPS 70W Applications", *J. Bridge Eng.*, **7**(1), 1-5.
Vander, V.G.J., De, B.J. and Wardenier, J. (1990), "Low cycle fatigue of tubular T- and X-joints", *Proceedings of the 3rd International Symposium on Tubular Structures*, Lappeenranta, Finland, September, pp. 605-616.
Yang, D.M. and Hancock, G.J. (2004), "Compression tests of high strength steel channel columns with interaction between local and distortional buckling", *J. Struct. Eng.*, **130**(12), 1954-1963.

CC